# Midtropospheric Anticyclonic Vortex Street Associated with a Cloud Band near a Cold Front

EIZI TOYODA,* HIROSHI NIINO, KAZUHISA TSUBOKI,+ AND RYUJI KIMURA

*Ocean Research Institute, University of Tokyo, Tokyo, Japan*

MASANORI YOSHIZAKI

*Forecast Research Department, Meteorological Research Institute, Tsukuba, Japan*

(Manuscript received 29 December 1997, in final form 3 July 1998)

ABSTRACT

The characteristics and formation mechanism of an anticyclonic vortex street of meso-$\beta$ scale, which appeared near a cold front around the Ryukyu Islands, Japan, on 11 April 1995, were examined by an analysis of observational data, a numerical simulation, and a linear stability theory.

The vortex street was generated near the midtroposphere on the north edge of a cloud band along the cold front. The diameter of individual vortices was 70 km, and the interval between vortices was 100–200 km. The phase speed of the vortices was nearly equal to the wind speed at the 400-hPa level.

The cloud band was accompanied by a weak wind region, in which the along-front wind was about 15 m $s^{-1}$ weaker than that in the environment. A region of large anticyclonic horizontal shear ($\sim 10^{-4}$ $s^{-1}$) existed on the north side of this weak wind region.

To examine a detailed structure and formation mechanism of the weak wind region, a numerical simulation was performed. Regions of active convection and convective cloud bands, associated with a convergence line of the surface wind, were reproduced at the position where they were observed. The weak wind region accompanied by the cloud band was also reproduced. A budget analysis of the along-front momentum equation shows that the weak wind region was produced by vertical advection of horizontal momentum in the convective cloud band, which is resolved by the 15-km grid interval of the numerical model.

The stability of the simulated along-front wind and temperature fields near the weak wind region was examined by a linear theory. It is found that there exist a number of growing modes, the disturbance kinetic energy of which is supplied by the kinetic energy of the basic flow (i.e., a barotropic instability). The fastest growing mode has a maximum amplitude at 450 hPa and is confined to the region of 450 hPa $\pm$ 100 hPa. The wavelength and phase velocity of the fastest growing mode agree well with those of the observed vortex street.

## 1. Introduction

Vortex disturbances of meso-$\beta$ scale (Orlanski 1975) are occasionally found in satellite cloud images and in radar reflectivity maps. Among various vortex disturbances observed around the Japan islands, two kinds of disturbances have been extensively studied: one is associated with the Japan Sea polar air convergence zone (JPCZ; Asai 1988), and the other is a vortex street behind an isolated mountainous island. The former has been observed since the 1960s by radar and surface observations. While a majority of the previous case studies (e.g., Miyazawa 1967; Asai and Miura 1981; Ninomiya and Hoshino 1990; Ookubo 1995) have analyzed an isolated vortex, Kibe and Matsumoto (1989) reported vortex streets (in their words, ''rope-shaped echo'') observed by a radar. All vortices reported in these studies had a cyclonic rotation.

A statistical study of Asai (1988) showed that these vortex disturbances occur mainly in winter and in two regions: the west coast of Hokkaido Island, and the southwest part of the Japan Sea between Hokuriku district and Korea. In these regions a near-surface convergence zone called the JPCZ frequently appears in winter. Asai also noted that similar vortex disturbances are commonly found over subarctic oceans. Asai and Miura (1981) speculated that the disturbances are caused by an instability of the strong horizontal shear associated

* Current affiliation: Division of Earth and Planetary Sciences, Graduate School of Sciences, Hokkaido University, Sapporo, Japan.
+ Current affiliation: Institute for Hydrospheric-Atmospheric Sciences, Nagoya University, Nagoya, Japan.

*Corresponding author address:* Dr. Eizi Toyoda, Division of Earth and Planetary Sciences, Graduate School of Sciences, Hokkaido University, Sapporo 060-0810, Japan.
E-mail: toyoda@ms.u-tokyo.ac.jp

with the JPCZ. A recent numerical study (Nagata 1993) supported the importance of horizontal shear.

A vortex street behind an isolated mountainous island, first noted by Hubert and Krueger (1962), is frequently observed behind Cheju Island (Tsuchiya 1969) and Rebun Island (Muramatsu 1971) during cold air outbreaks. These islands have conical-shaped mountains near their centers. The depth of the convective mixed layer that develops during a cold air outbreak is typically about half as high as the mountain. The height of the vortices nearly corresponds to the depth of the convective mixed layer. The vortex street consists of alternating cyclonic and anticyclonic vortices. A satellite image of the vortex street shows a close resemblance to the von Kármán vortex street observed in a laboratory experiments (e.g., Hino 1992). The generation mechanism of the former, however, seems to be different from that of the latter and is under active investigation (e.g., Schär and Durran 1997).

There have been several other vortex disturbances that are not classified into one of these two categories. Yasuda (1974) reported a cyclonic vortex of 60-km diameter near the Baiu front in the radar reflectivity map at Naze. The top of the vortex reached 5–7 km in height. The Niigata Local Meteorological Observatory (1972) observed an anticyclonic vortex of about 50 km in diameter with Mount Yahiko radar in September 1972. The vortex was located on the cold side of a cold front. Nyuda (1974) reported an anticyclonic vortex of about 100 km in diameter observed by Tojimbo radar in July 1972. The vortex was on the warm side of a cold front. Although the vertical extent of the vortex was not described explicitly, the elevation angle of the radar suggests that the vortex formed in the lower troposphere. Using satellite images, Lyons (1988) reported a cyclonic vortex street in the northeast Pacific Ocean, far west of Mexico. The interval of vortices was about 300 km. However, the formation mechanism of these vortices was not examined because of lack of observational data.

On 11 April 1995, a remarkable vortex street was observed in Geostationary Meteorological Satellite (GMS) infrared images along a cold front near the Ryukyu Islands (southwest of Kyushu Island). The location and the season of the vortex street were clearly different from the von Kármán and JPCZ vortices. The vortex street of this study is unique in the following respects. First, each vortex had an anticyclonic rotation, which was opposite to the vorticity of the wind shear in the lower troposphere. Second, the horizontal scale of the vortex was small (about 50 km). Third, the cloud associated with the vortices was quite high (~7 km in height). If such midtropospheric vortices occur frequently, they may play an important role in horizontal mixing of mass and momentum in the free atmosphere.

The purpose of the present study is to clarify the characteristics of the vortices and their formation mechanism based on an analysis of observational data, a numerical simulation, and a theoretical stability analysis.

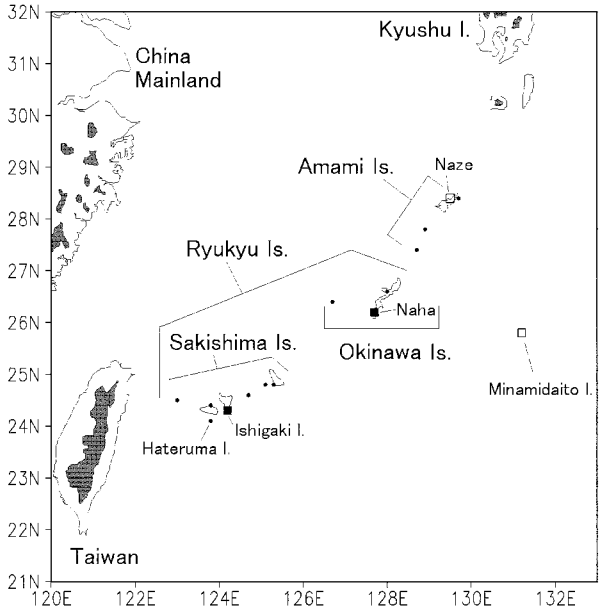


FIG. 1. Geographical map of the analysis region. Hatched areas are higher than 1000 m. Solid circles indicate surface stations, open squares upper-air–surface stations, solid squares upper-air–surface–radar stations.

Since the vortex street was at the northern edge of a convective cloud band of more than 1000 km in length, we are particularly interested in the relationship between the vortices and the cloud band.

In section 2, the observational data are analyzed to reveal the characteristics of the vortices. The environmental field of the vortex street is numerically simulated in section 3, and the stability of the environmental field is examined in section 4. The results are discussed in section 5.

## 2. Observational analysis

### *a. Data and analysis region*

Figure 1 shows a geographical map of the region for the present study. Data from the surface stations (including airport observatories), upper-air sounding stations, meteorological radar sites, GMS infrared and visible images, and objective analyses of the Japan Meteorological Agency (JMA) were analyzed. The locations of the stations and radar sites are shown in Fig. 1. Wind traces were available from all the surface stations. Upper-air soundings are made at Naze, Naha, Minamidaito Island, and Ishigaki Island, where wind profiles are observed at 0000, 0600, 1200, and 1800 UTC, and temperature and humidity profiles at 0000 and 1200 UTC.

Radar reflectivity data are available every 3 h. When heavy precipitation occurred within the detection range of the radar, the sampling interval was decreased to 7.5 min. GMS images were available every hour. Since the

vortex street appeared during nighttime, infrared images were mainly used for the present analysis. Objective analysis data of the Japan area (JANAL) are available twice a day (at 0000 and 1200 UTC) from JMA. Its horizontal grid size at 26°N is 31 km.

### *b. Characteristics of the vortex street*

The vortex street appeared between 22° and 26°N, at the northern edge of a cloud band associated with a cold front, between 1200 and 1800 UTC 11 April 1995. Figure 2 shows hourly GMS infrared images near the cloud band during this period. The distance between vortices was 100–200 km. Each vortex moved northeastward at a speed of 30 m $s^{-1}$. The most remarkable vortex, the diameter of which was 70 km, appeared around 1200 UTC at (23°N, 124°E) and moved to (27°N, 132°E) in 6 h before it disappeared from the GMS image at 1900 UTC.

Figure 3 shows the brightness temperature ($T_{bb}$) of the GMS infrared image at 1600 UTC. At the top of the vortex-shaped cloud, $T_{bb}$ was −30°C. This corresponds to the temperature at about 350 hPa, and also to the top of the high-humidity region in the upper-air sounding at 0000 UTC 11 April 1995 at Naha. The lower clouds (temperature higher than 0°C) showed no vortexlike pattern.

The PPI images of the radar reflectivity at 1500 UTC (Fig. 4) indicate that precipitation was located along the southwest end of the cloud band, but not near the vortex cloud. Thus, it is likely that the cloud particles near the vortices simply played a role of tracer of the midtropospheric wind.

A convective cloud system that has a narrow triangular shape in its southwest end, as shown in Fig. 3, is called a ''tapering cloud.'' In the present case, the tapering cloud is observed over the sea east of Taiwan and Sakishima Islands. A statistical study on tapering clouds around Japan by Itoh et al. (1992) showed that they do occur most frequently in this region. Akaeda and Sakakibara (1996) reported a case study on such a tapering cloud with heavy rain.

### *c. Synoptic condition*

Figure 5 shows a surface synoptic chart at 1200 UTC 11 April 1995, when the vortex street was observed. Two extratropical cyclones were located south of Shikoku Island. Each accompanied a cold front. The vortex street appeared near the southwest end of the southern front.

On 10 April 1995, a cold front was located between the Okinawa Islands and south China. A cyclone developed along the front at 1800 UTC 10 April and moved northeastward while developing. The cyclone passed over the Amami Islands at 0000 UTC 11 April. At 1200 UTC 11 April, another cyclone and an associated front appeared (Fig. 5). The surface wind indicates that the two fronts were clearly identified to the east of the 130°E longitudinal line: the northern front was identified as a boundary between regions of southwesterly and northwesterly winds, while the southern front was identified as a convergence zone in the southwesterly region. On the west side of 130°E (i.e., around the Ryukyu Islands) the northern front was indistinct, and the southern front was formed between two different winds. The mesoscale structure of this frontal zone will be described in the next section.

At 0000 UTC 12 April, a cloud system associated with the southern front passed over the Ryukyu Islands. After 24 h, the front was located 400 km southeast of Okinawa Island. The average speed of the front (normal to front) was 17 km $h^{-1}$ (5 m $s^{-1}$).

### *d. Mesoscale structure of the frontal zone*

Figure 6 shows a series of GMS infrared images between 1800 UTC 10 April and 1200 UTC 11 April. The cloud system associated with the frontal zone was 600 km in width and consisted of three cloud bands of about 100 km in width, with an interval of roughly 200 km. The bands are hereafter denoted as cloud bands A, B, and C (see Fig. 6c). Each cloud band had a precipitating region on its southwest end. The precipitating region consisted of several broken-line structures of about 200 km in length and 10 km in width. They are hereafter referred to as cloud lines. Such a broken-line structure of the precipitation region was observed during the developing stage of cloud bands (cloud band B had two developing stages: one at 0300 UTC 11 April and the other at 1200 UTC 11 April). This also supports the notion that the cloud band was produced by an advection of cloud particles from the precipitating region.

Radar reflectivity data show that cloud lines in cloud bands A and B had heavy precipitation (Fig. 4). These cloud lines were located along the south edge of the frontal zone and corresponded to the surface cold front. During the passage of these cloud lines, the surface wind turned from southerly to northerly (cf. Figs. 6a and 6c) and a strong gust of more than 20 m $s^{-1}$ was observed at Hateruma Island. This cold front is identified as a convergence zone between the northerly wind and the southeasterly one that initially prevailed over this region.

### *e. Wind distribution near the front*

Three of the four upper-air stations in the analysis region (Fig. 1), Ishigaki Island, Naha, and Naze, are aligned in the southwest–northeast direction, which is nearly parallel to the front. Minamidaito Island is located approximately 400 km southeast of the line formed by the other three stations. Assuming that the structure of the frontal zone is time independent and uniform in the along-front direction, and using a time–space conversion (Fujita 1963), we can then study the

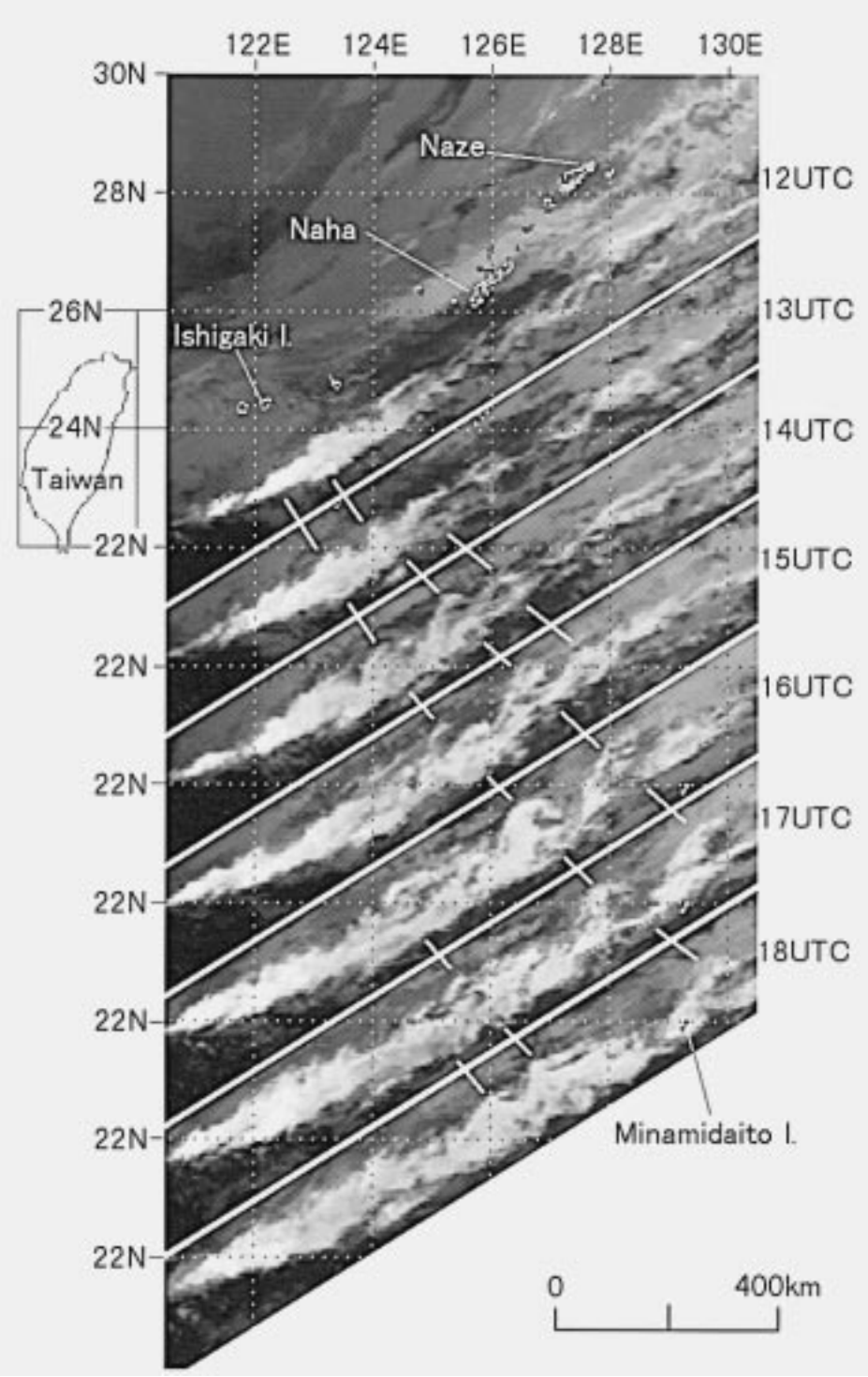


FIG. 2. Hourly GMS infrared images near the vortex street between 1200 and 1800 UTC 11 April 1995. Each segment has a latitudinal width of 2° (220 km).

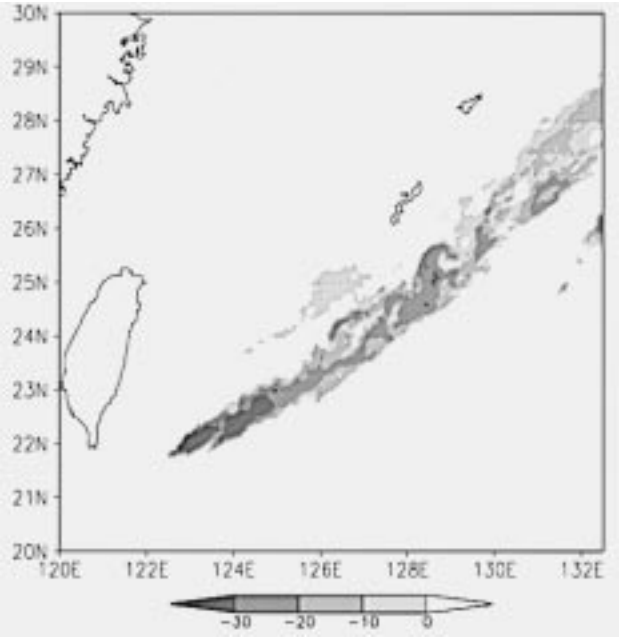


FIG. 3. GMS infrared image at 1600 UTC 11 April 1995. Brightness scale is corresponding blackbody temperature (°C).

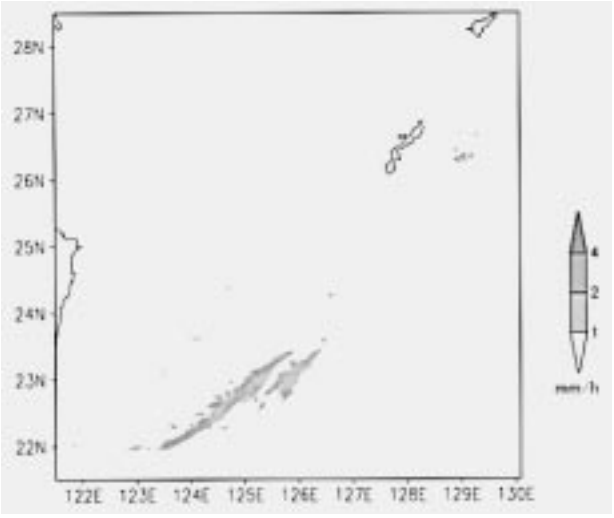


FIG. 4. Radar reflectivity map at 1500 UTC 11 April 1995 from Naha Island and Ishigaki Island radars. Degree of shading denotes corresponding rainfall intensity.

cross-frontal structure of the frontal zone. Since the front moved at a constant speed of 5 m $s^{-1}$ toward an azimuth of 150°, the time–space conversion gives a horizontal resolution of 100 km for the 6-h interval of the upper-air soundings.

Figure 7 shows a time–height cross section of the along-front wind observed at Naha for 48 h from 0600 UTC 10 April 1995. The shaded areas indicate regions of high relative humidity (>70%), which may be assumed to be cloud regions. Cloud band A passed over Naha around 0000 UTC 11 April. During the passage of cloud band A, a remarkably weak wind was observed in the middle troposphere (300–700 hPa). The top of the weak wind region corresponds to that of the cloud. A strong horizontal wind shear with significant anticyclonic vertical vorticity is noted on the northwest side of the weak wind region. The minimum vertical relative vorticity was $-1.1 \times 10^{-4}$ $s^{-1}$. The height of the cloud region estimated from the upper-air soundings coincided with that of the vortex cloud estimated from the GMS cloud-top temperature. The wind speed in the weak wind region ($\sim$30 m $s^{-1}$) nearly coincides with the translational speed of the vortices.

Figure 8 shows a time–height cross section of potential vorticity calculated from the wind data in Fig. 7 and 12-hourly thermodynamic sounding data. Potential vorticity here is calculated as

$$P = -g\frac{\partial u}{\partial p}\frac{\partial \theta}{\partial y} - g\left(f - \frac{\partial u}{\partial y}\right)\frac{\partial \theta}{\partial p}, \qquad (1)$$

where $f = 2\Omega \sin\varphi$ is Coriolis parameter, $\theta$ is the potential temperature, $u$ is the along-front wind, and $y$ is cross-frontal length estimated from the time–space conversion. The term including along-frontal derivative in the original definition of potential vorticity was neglected, since we cannot evaluate it from soundings at a single observational point.

Minimum potential vorticity exists in the anticyclonic shear region and the line that connects minima of potential vorticity is nearly vertical. A detailed examination reveals that the minima of potential vorticity is mainly caused by the distribution of $(f - \partial u/\partial y)$ but not by that of $\partial\theta/\partial p$. Thus, a possibility of barotropic instability is suggested.

Right below the weak wind region, there exists a region of relatively strong wind. Coexistence of the weak wind region in the upper parts and the strong wind region in the lower parts of the cloud band suggests a vertical mixing of horizontal momentum by convection. A similar weak wind region during a passage of a cloud band was also observed in the upper-air soundings at Ishigaki and Minamidaito Islands (not shown).

## 3. Numerical simulation

As we have shown in section 2, the generation of the vortex street appears to be associated with the weak wind region. The spatial resolution of the observational data, however, is typically 100 km and is not sufficient to examine the generation mechanism of the vortices. Although the JANAL data have a spatial resolution of 31 km, they are essentially based on the upper-air observations and are not capable of obtaining much improvement in the spatial resolution. In order to investigate the generation mechanism and the detailed structure of the weak wind region, a numerical simulation was performed.

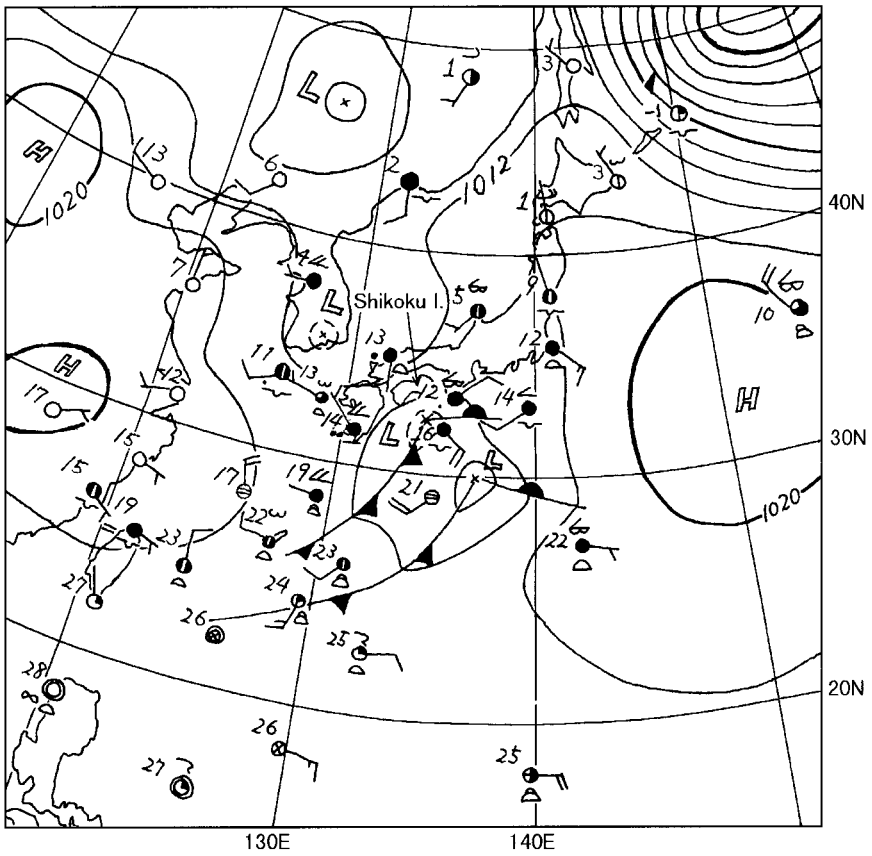


FIG. 5. Synoptic chart at 1200 UTC 11 April 1995. Surface wind vectors full barb = 5 m s$^{-1}$; half-barb = 2.5 m s$^{-1}$. Cloud cover (octants) are shown within station circle.

### *a. Description of numerical model*

A modified version of the 1988 Japan Spectral Model (JSM) (Segami et al. 1989), a former numerical prediction model of JMA, was used for the present simulation. JSM is a $\sigma$-coordinate primitive equation model. The vertical resolution was increased to 23 levels (cf. 19 levels in the original model). In the horizontal directions, the spectral method is used with time-dependent boundary condition (Tatsumi 1986). The polar stereographic projection is adopted. Here 129 $\times$ 129 grid points were used with maximum wavenumbers of 83 $\times$ 83. An elliptic wavenumber truncation was used. A one-way nesting of two models with grid sizes of about 23 and 15 km was adopted. Hereafter, wherever the term ''grid size'' is used, it denotes the value at 26°N [grid size is inversely proportional to the map factor $2/(1 + \sin\varphi)$, where $\varphi$ is the latitude]. Details of the nesting procedure will be described in the next section. Time integration was made with a semi-implicit leapfrog method.

The parameterizations of the physical processes included in JSM are Mellor and Yamada's (1974) turbulent closure scheme for vertical diffusion in the planetary boundary layer, large-scale condensation, moist convective adjustment (Gadd and Keers 1970), and raindrop evaporation (Ogura and Takahashi 1971).

For the horizontal diffusion, the model uses a biharmonic diffusion proportional to $\nabla^4$. The coefficient of biharmonic diffusion was set to $2.7 \times 10^{12}$ m$^4$ s$^{-1}$ for the 15-km mesh model. This is equivalent to an ordinary harmonic diffusion of $5.3 \times 10^4$ m$^2$ s$^{-1}$ at the truncation wavenumber (the wavelength of 47 km).

The lateral boundary conditions were provided from JANAL data, instead of from the Asian Spectral Model in the original JSM.

### *b. Initial field and computation procedure*

The JANAL data at 1200 UTC 10 April 1995, 24 h before of the appearance of the vortex street, was used as the initial field of the model. The model was then run for 36 h. First, the 23-km mesh model was run with the lateral boundary conditions supplied from time-interpolated JANAL data. The result is used as the initial and lateral boundary conditions for the 15-km mesh model. The calculation domains of the two models are shown in Fig. 9.

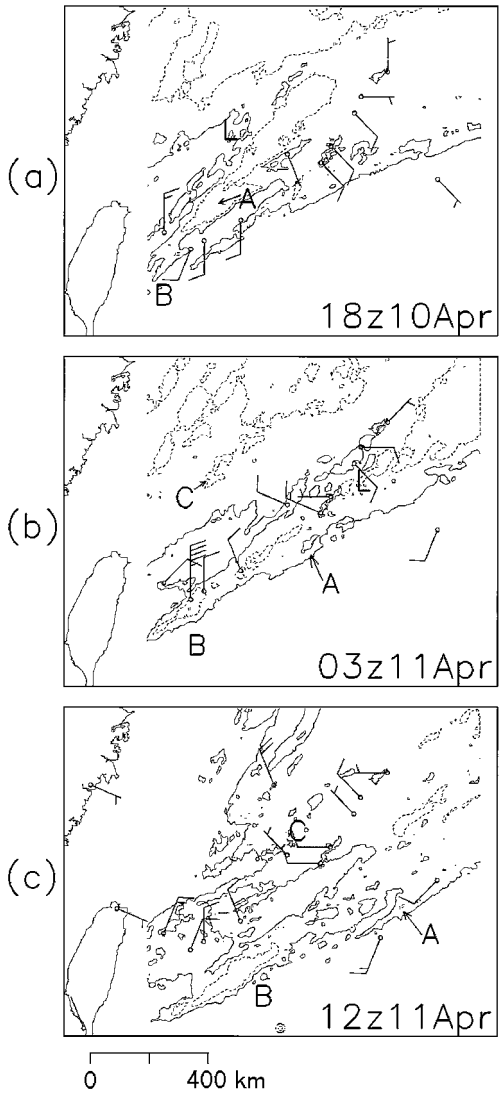


FIG. 6. Surface winds (barbed arrow) and GMS infrared images; (a) 1800 UTC 10 April 1995, (b) 0300 UTC 11 April 1995, and (c) 1200 UTC 11 April 1995. Shaded areas denote temperature less than 10°C, and dashed lines are contours of −20°C. Wind vectors are the same as in Fig. 5.

### c. Results of simulation

Figure 10a shows the horizontal cross section of the along-front wind and region of high relative humidity (>70%) at 400 hPa at 0800 UTC 11 April (20 h after the start of integration; hereafter, time will be given in the corresponding UTC instead of the integration time). Two regions of high relative humidity were predicted by the model. Since the regions of high relative humidity may be regarded as cloud areas, these regions will be referred to as cloud bands $\beta$ and $\gamma$. They correspond well to the observed cloud bands B and C (Fig. 6).

Figure 10b shows the vertically averaged diabatic heating rate, which is a good measure of the precipitation. Surface wind vectors are also shown. Two precipitation regions exist in the southwest end of the cloud band $\beta$. The wind direction near the cloud band at the 400-hPa level is almost in the along-front direction (azimuth of 240°). The cloud bands also extend nearly parallel to the front. The regions of high relative humidity were generated in the precipitation regions and were advected by the upper-level wind. These features agree with those of the observed cloud band B (see section 2).

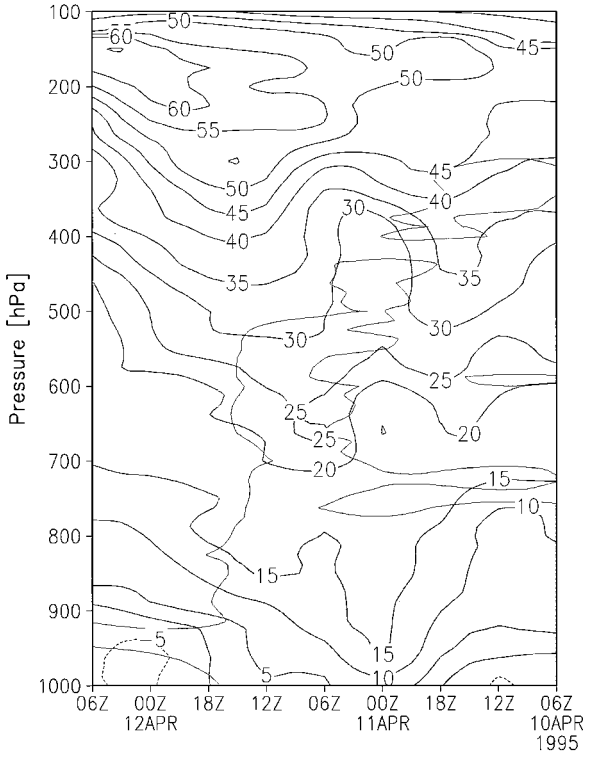


FIG. 7. Time–height cross section of the along-front wind (m s$^{-1}$) at Naha. Shaded area denotes high relative humidity (>70%).

Now let us compare the behavior of the simulated cloud band $\beta$ with the observed cloud band B. Precipitation associated with the cloud band $\beta$ began to develop at 1900 UTC 10 April at 23°N, 122°E (east of Taiwan), which is about 100 km south of the observed cloud band B at this time (Fig. 6b). Cloud band $\beta$ moved southeastward more slowly than cloud band B did, and it was eventually located at nearly the same position as the cloud band B at 0800 UTC 11 April. However, the precipitation regions associated with both cloud bands were about 200 km apart: the precipitation region of the cloud band B was located at (24°N, 124°E) in the south of the Sakishima Islands (Fig. 6f), while that of the cloud band $\beta$ was at (23°N, 124°E) and (25°N, 127°E) (Fig. 10b).

Except for the difference of about 200 km in their locations, cloud band $\beta$ has many similarities to cloud band B: the surface wind field indicates that both exist in the convergence zone between northwesterly winds

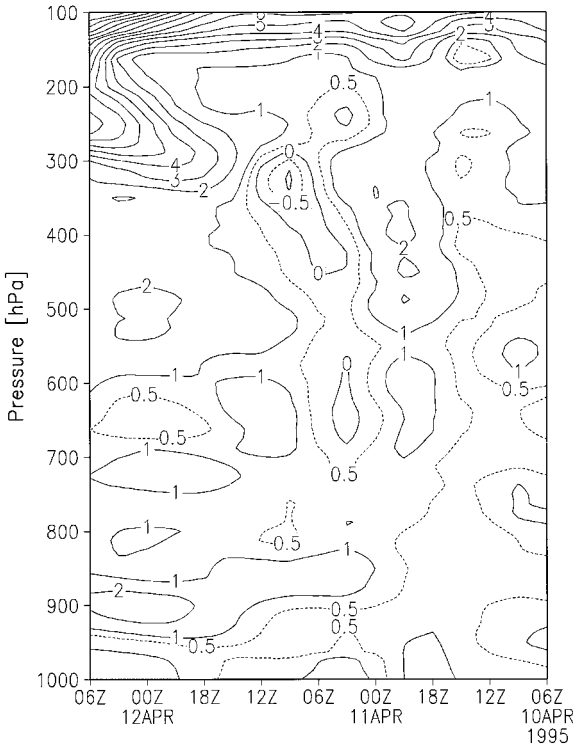


FIG. 8. Time–height cross section of the potential vorticity at Naha. Shaded area denotes negative potential vorticity. (The unit is PVU $\equiv 10^{-6}$ m$^2$ kg$^{-1}$ s$^{-1}$ K.)

and prevailing southeasterly winds to the southwest of the Ryukyu Islands. The cross-front vertical section (shown by the broken line on Fig. 10a) of along-front wind at the same time (0800 UTC 11 April) is shown in Fig. 11. The abscissa, which is hereafter referred to as the $y$ coordinate, is a distance from (22.5°N, 129°E) toward the direction of 330°. It is seen that a weak wind region of about 200 km in width is associated with the cloud band $\beta$ at $y = 350$ km between 600 and 400 hPa. The maximum velocity deficit in the weak wind region was 10 m s$^{-1}$. These characteristics of the weak wind region are similar to the observed ones (see section 2). Similarly, the simulated cloud band $\gamma$ compares well with the observed cloud band C.

Figure 12 shows the diabatic heating rate on the same cross section. Diabatic heating in cloud band $\beta$ is more active than in cloud band $\gamma$. In fact, the observed radar echo pattern was stronger in cloud band B than in cloud band C.

Thus, the two weak wind regions associated with the cloud bands were satisfactorily simulated, except for differences of about 200 km in the locations.

### *d. Formation mechanism of the weak wind region*

Now we will examine the formation mechanism of the weak wind region. To this end, a budget analysis of the along-front momentum is made. The acceleration in the along-front direction was divided into six terms:

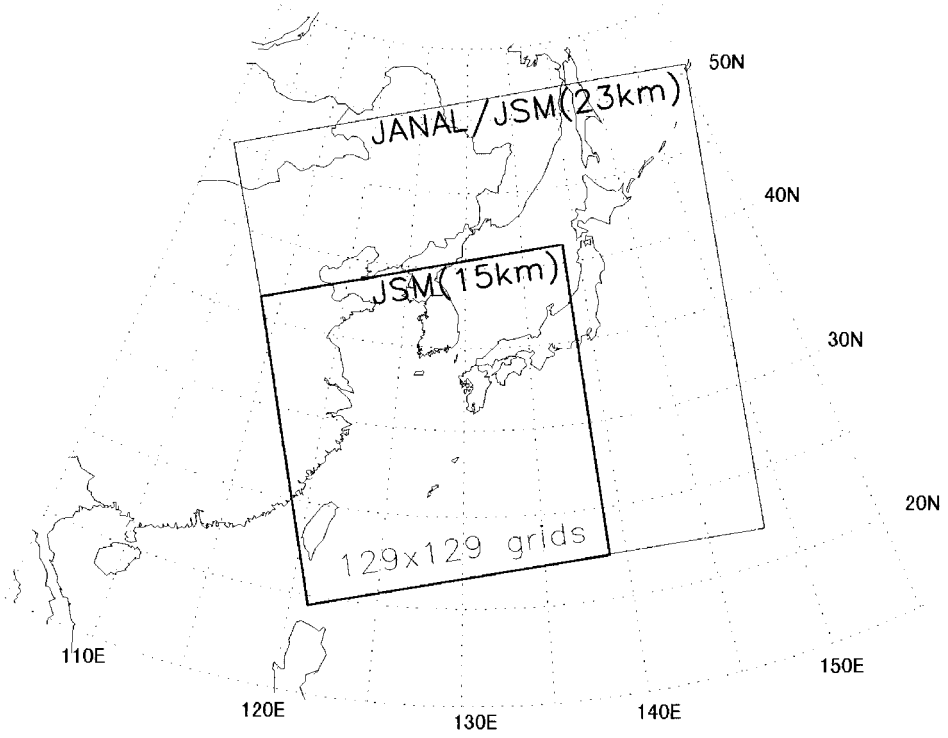


FIG. 9. The domains for the numerical simulation. The thin lines show the domain for JANAL and the 23-km mesh model, and the thick lines for the 15-km mesh model.

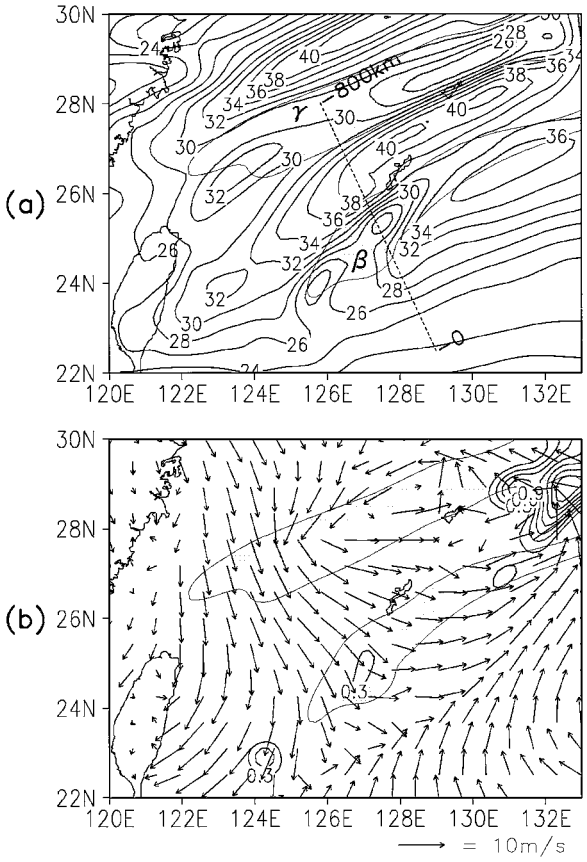


FIG. 10. Simulated cloud bands at 0800 UTC 11 April 1995. Shaded area denotes the region of high humidity (>70%). (a) Along-front wind at 400-hPa level; the broken line denotes the cross section used in Fig. 11. (b) Diabatic heating rate averaged over 300–1000-hPa levels (K $h^{-1}$). Arrows denote the surface wind vector (m $s^{-1}$).

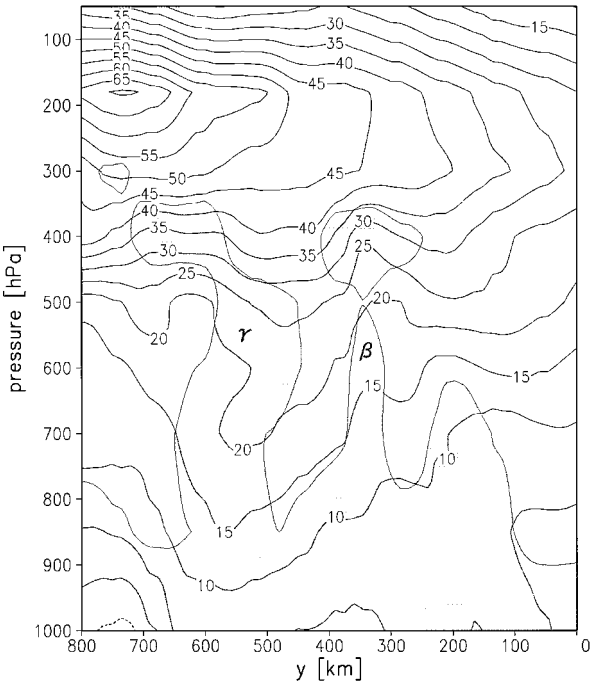


FIG. 11. Vertical cross section of along-front wind (m $s^{-1}$) at 0800 UTC 11 April 1995, along the broken line in Fig. 10a. Shaded area indicates high relative humidity (>70%).

pressure gradient force, Coriolis force, vertical and horizontal advection of momentum, and vertical and horizontal diffusion of momentum.

JSM uses a spectral method with time-dependent lateral boundary conditions. Accordingly, the ''additional bases'' (Tatsumi 1986) are used to describe the time-varying boundary conditions. The semi-implicit scheme is used for the time integration. Therefore, the sum of the six terms does not agree exactly with the acceleration, though the difference is generally small.

Figure 13 shows the contribution of each term to the acceleration of the along-front velocity in the same cross section and at the same time as Fig. 11. At 0800 UTC 11 April, the weak wind region was developing, and the total acceleration was negative in the region (Fig. 13a). Dashed lines denote the wind isotach near the weak wind region. Among the six terms, the pressure gradient force and the Coriolis force are the largest and are ~10 m $s^{-1}$ $h^{-1}$. They are, however, nearly in balance and their sum is about 0–2 m $s^{-1}$ $h^{-1}$ except above 300 hPa, where the wind was not along-front (Fig. 13b). It is also seen that the spatial pattern of the sum of the pressure gradient force and the Coriolis force does not match that of the weak wind region.

The horizontal advection of momentum is the third largest (Fig. 13c). It is negative on the advancing side of the weak wind region (right in the figure) and was positive behind. This means that this term simply represents a translation of the weak wind region southeastward without intensification.

The vertical advection, the fourth largest term, has a significant negative value in the region (Fig. 13d). It shows a similar spatial pattern to that of the weak wind region and its minimum value reaches −2 m $s^{-1}$ $h^{-1}$. Furthermore, the vertical advection term became small after 1200 UTC 11 April, when the weak wind region stopped developing.

The vertical diffusion of momentum is at most 0.2 m $s^{-1}$ $h^{-1}$ in its absolute value above 900 hPa (Fig. 13e). The horizontal diffusion is concentrated in the middle troposphere. Its absolute value is less than 0.3 m $s^{-1}$ $h^{-1}$ and has even positive value in the weak wind region (Fig. 13f). Thus, diffusion of momentum is not important in the production of the weak wind region.

The above analysis shows that the weak wind region in the numerical model is generated by the vertical advection of horizontal momentum. This vertical advection is caused by the updraft in the convective cloud band, which was resolved with the 15-km mesh model. The numerical model simulated the configuration of the

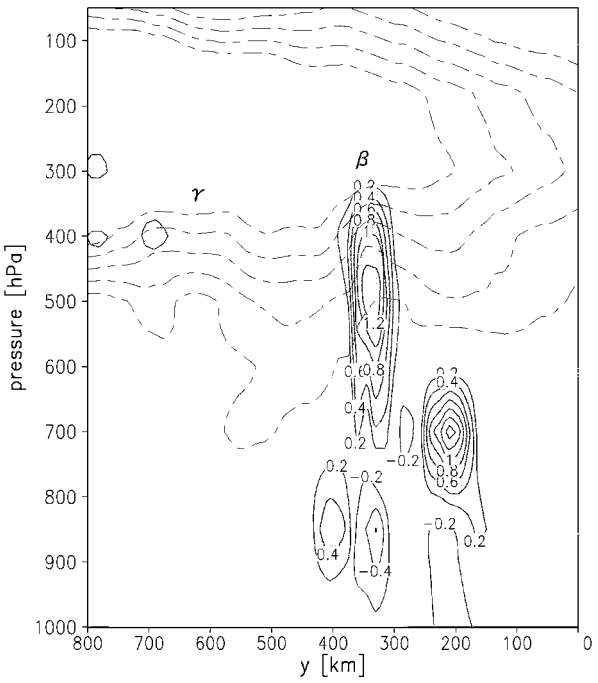


FIG. 12. Same as Fig. 11 except for diabatic heating rate between 0700 and 0800 UTC 11 April 1995. The region of absolute value $>0.2$ K h$^{-1}$ is shaded. Dotted lines are contours for the along-front wind (same as Fig. 11).

observed cloud bands quite satisfactorily, as described in section 3c. In particular, the observed feature that the weak wind region exists between 600 and 400 hPa in the cloud band was well reproduced by the model. We conclude, therefore, that the weak wind region in the real atmosphere was also generated by the vertical transport of the along-front momentum by the convective cloud band.

## 4. Linear stability theory

In the previous section, the cloud bands and the associated weak wind regions were successfully reproduced in the numerical model. Though the horizontal grid size of the model (15 km) is not sufficient to describe the formation mechanism of the vortex street, the simulation gives a much finer structure of the environmental field of the vortices than the observation does. Since the observed vortex street is considered to be caused by a hydrodynamic instability, we will examine the stability of the numerically simulated environmental field.

### *a. Basic equations and formulation*

We use the primitive equation system in the pressure coordinate and ignore viscosity and diabatic heating. The beta effect is neglected since we are interested in disturbances whose horizontal scale is about 100 km. Let us take the $x$ axis parallel to the front (northeastward) and the $y$ axis perpendicular to it (northwestward). The governing equations are given by

$$\partial_x u + \partial_y v + \partial_p \omega = 0, \tag{2}$$

$$\partial_t u + u\partial_x u + v\partial_y u + \omega\partial_p u - fv = -\partial_x \Phi, \tag{3}$$

$$\partial_t v + u\partial_x v + v\partial_y v + \omega\partial_p v + fu = -\partial_y \Phi, \tag{4}$$

$$\partial_p \Phi = -\frac{RT}{p}, \tag{5}$$

$$\partial_t T + u\partial_x T + v\partial_y T - \omega\left(\frac{RT}{c_p p} - \partial_p T\right) = 0, \tag{6}$$

where $p$ is the pressure coordinate, $t$ time, $(u, v, \omega)$ the velocity components in the $(x, y, p)$ directions, $\Phi$ the geopotential, $T$ the temperature, $f$ the Coriolis parameter, $R$ the gas constant for air ($2.870 \times 10^2$ Pa m$^3$ K$^{-1}$), and $c_p$ specific heat at constant pressure ($3.5R$). Partial derivatives are written as $\partial_x \equiv (\partial/\partial x)$.

We assume that the wind profile of the basic field is time independent and is a function of $y$ and $p$:

$$(\overline{u}, \overline{v}, \overline{\omega}) = (\overline{u}(y, p), 0, 0). \tag{7}$$

Geopotential $\overline{\Phi}$ in the basic state is taken from the hydrostatic balance [(5)]. The basic-state temperature $\overline{T}$ is obtained so as to satisfy the thermal wind relationship:[1]

$$\partial_y \overline{T} = \frac{pf}{R}\partial_p \overline{u}. \tag{8}$$

Let us consider a channel along the $x$ axis. Pressures at the top and bottom of the channel are 0 and $\Pi$, and the width of the channel is $2bL$, where $L$ is the characteristic width of the horizontal wind profile. The lateral and vertical boundary conditions are

$$v = 0 \quad \text{at } y = -bL, +bL \tag{9}$$

and

$$\omega = 0 \quad \text{at } p = 0, \Pi. \tag{10}$$

If the lateral walls are sufficiently distant from the horizontal shear zone ($b \gg 1$), the effect of the vertical walls on the stability is generally small [Yanai and Nitta (1968) concluded that the stability of a shear layer between two uniform flows is well described by placing two rigid walls at $y = \pm 2L$]. The vertical boundary condition (10) is equivalent to placing a horizontal wall at the bottom isobaric level $p = \Pi$ [at the top of air $p = 0$, the vertical boundary condition (10) holds without

[1] We have also made the instability calculation based on the temperature field directly taken from the output of the JSM. Since the result differs very little from those for the basic temperature $\overline{T}$ given by (8), only the result for the geostrophically balanced temperature field will be presented in the following.

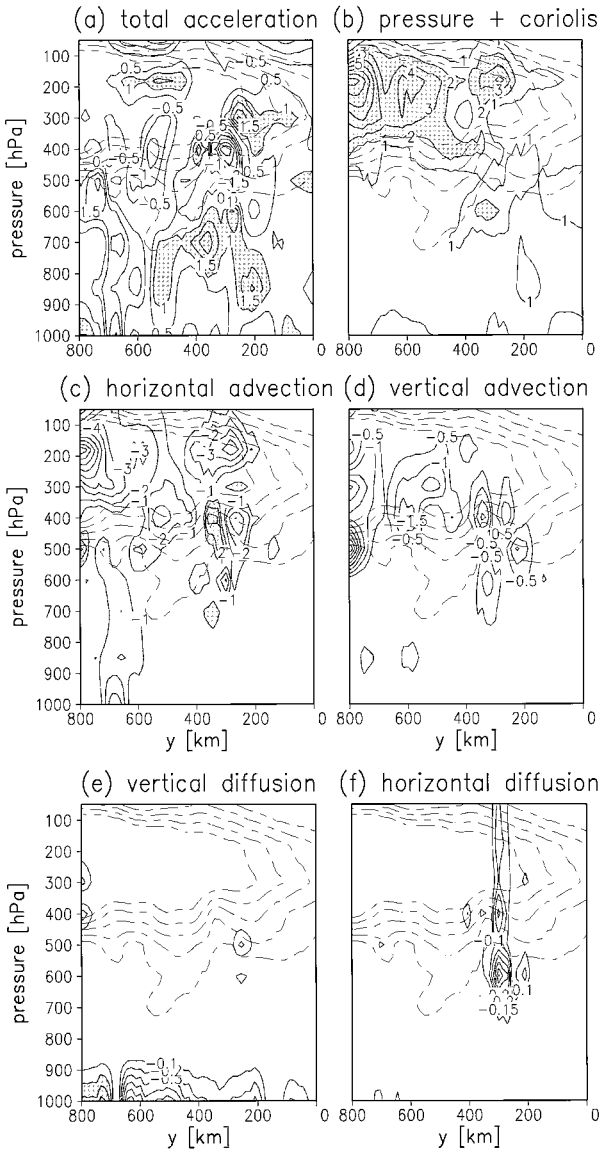


FIG. 13. Vertical cross section of along-front acceleration (m $s^{-1}$ $h^{-1}$) at 0800 UTC 11 April 1995; (a) the total acceleration, (b) the sum of pressure gradient force and Coriolis force, (c) vertical advection of momentum, (d) horizontal advection of momentum, (e) vertical diffusion of momentum, and (f) horizontal diffusion of momentum. Shaded area denotes large absolute value of acceleration. Dotted lines are contours for the along-front wind (same as Fig. 11).

any assumption, since there is no vertical flow]. In the present study $\Pi$ is taken to be 1000 hPa. As will be shown later, the vertical extent of the fastest growing mode is small and the influence of vertical boundary conditions on the mode is small.

Let us assume that the variables $u$, $v$, $\omega$, $\Phi$, and $T$ in (2)–(6) are divided into the basic field and a perturbation as $u = \overline{u} + u'$ and so on. If these expressions are substituted into the governing equations and the resulting equations are linearized with respect to the perturbations ($u'$, $v'$, $\omega'$, $\Phi'$, $T'$), we have

$$\partial_x u + \partial_y v + \partial_p \omega = 0, \tag{11}$$

$$\partial_t T + \overline{u}\partial_x T + v\partial_y \overline{T} - \omega \overline{S} = 0, \tag{12}$$

$$\mathrm{Ro}(\partial_t u + \overline{u}\partial_x u + v\partial_y \overline{u} + \omega\partial_p \overline{u}) - v = -\partial_x \Phi, \tag{13}$$

$$\mathrm{Ro}(\partial_t v + \overline{u}\partial_x v) + u = -\partial_y \Phi, \tag{14}$$

$$\partial_p \phi = -\frac{T}{p}, \tag{15}$$

where the horizontal length is scaled by $L$, the vertical scale by $\Pi$, the horizontal velocity by $U$, time by $L/U$, geopotential by $LUf$, and temperature by $(LUf)/R$. The prime ($'$) has been dropped for simplicity. Here $\mathrm{Ro} \equiv U/(fL)$ is a Rossby number and

$$\overline{S} \equiv \frac{R\overline{T}}{c_p p} - \partial_p \overline{T}$$

is the static stability in pressure coordinate. The boundary conditions in nondimensional form are

$$v = 0 \quad \text{at } y = -b, +b \tag{16}$$

and

$$\omega = 0 \quad \text{at } p = 0, 1. \tag{17}$$

Since Eqs. (11)–(15) and the boundary conditions (16) and (17) are linear, any disturbance can be expressed as a superposition of normal modes with different wavenumbers in the $x$ direction. Strictly speaking, the continuum modes (Case 1960), a superposition of which varies algebraically with time, must be added to describe completely the behavior of an arbitrary initial disturbance. If an exponentially growing normal mode exists, however, the continuum modes will eventually be dominated by the growing mode and will become unimportant.

We assume that the normal modes have the form

$$\begin{pmatrix} u \\ v \\ \omega \\ T \\ \Phi \end{pmatrix} = \begin{pmatrix} u(y, p) \\ v(y, p) \\ \omega(y, p) \\ T(y, p) \\ \Phi(y, p) \end{pmatrix} \exp[ik(x - ct)], \tag{18}$$

where $k$ is the wavenumber in the $x$ direction and $c$ the eigenvalue. The eigenvalue $c = c_r + ic_i$ is generally complex, where $c_r$ gives the phase velocity and $kc_i$ the growth rate. Here $1/(kc_i)$ is the $e$-folding time. When there exists a disturbance with $c_i > 0$ for some $k$, the basic field is unstable.

Substituting (18) into (11)–(17), we obtain a two-dimensional eigenvalue problem for given $k$ and Ro. The eigenvalue problem was solved numerically by a finite difference method. Details of the computational procedure are described in appendix A.

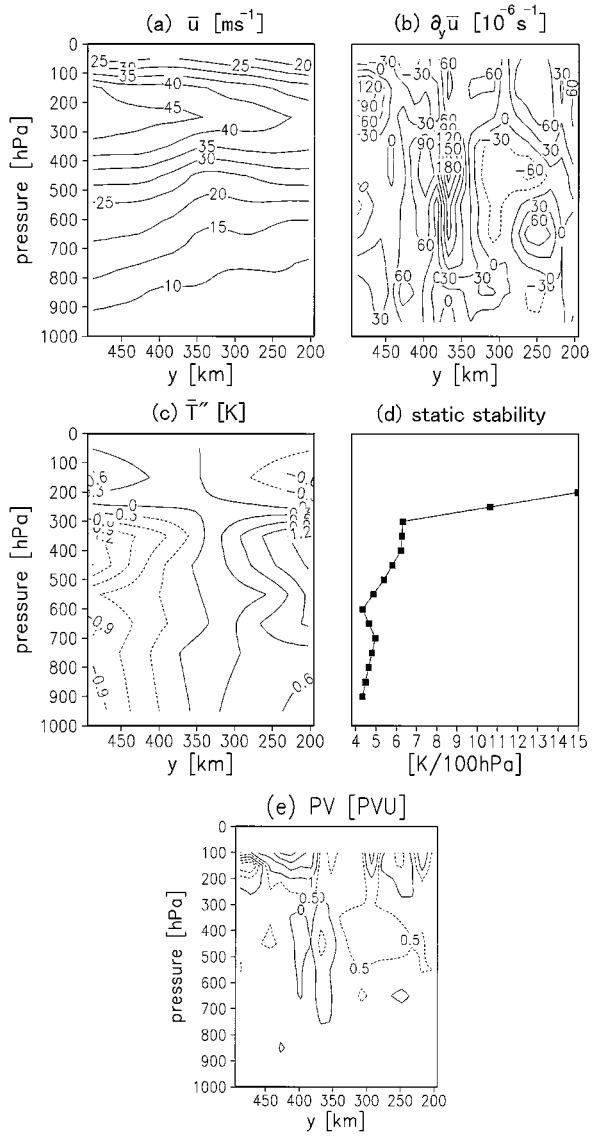


FIG. 14. Basic field of the two-dimensional model; (a) along-front wind $\overline{u}$ (m s$^{-1}$), (b) horizontal wind shear $\partial_y\overline{u}$ ($10^{-6}$ s$^{-1}$), (c) temperature anomaly from horizontal average $\overline{T}''$ (K), (d) vertical profile of static stability $\overline{S}$ [K (100 hPa)$^{-1}$], and (e) potential vorticity PV (PVU).

### b. Stability of two-dimensional wind profile

The two-dimensional along-front wind and temperature field in the cross section indicated by the broken line in Fig. 11 is used as the basic state for the stability analysis (Fig. 14). The horizontal and vertical ranges of the channel for the stability analysis are $y = 200\sim500$ km and $p = 1000\sim0$ hPa. This covers the whole weak wind region associated with cloud band $\beta$. The velocity deficit in the weak wind region (10 m s$^{-1}$) was used as the scaling velocity $U$ and the half-width of the weak wind region (100 km) as the scaling length $L$. This gives a nondimensional width $b$ of 1.5. The numbers of grid points used were 20 and 10 in the horizontal and vertical directions, respectively.

Figure 14e shows the potential vorticity distribution of the basic state. Considering that Fig. 8 is obtained by the time–space conversion of a single observation point, we think that the potential vorticity in Fig. 14e is reasonably similar to that in Fig. 8.

Figure 15 shows the dispersion relation obtained from the eigenvalue problem. The number of eigenmodes is equal to the degrees of freedom of the system, which is $3 \times 10 \times 20 - 20 = 580$ (see appendix A). The number of growing modes depends on the wavenumber and does not exceed 50. These growing modes have been denoted $T_1$, $T_2$, . . . in the order of their maximum growth rates.

Table 1 shows characteristics of several significant modes. For all these modes, the $C(\overline{K}, K')$ term (see Fig. B1) is dominant among the energy conversion terms: that is, these modes result from barotropic instability.

Figure 16 shows the vertical structures of modes $T_1$, $T_2$, and $T_3$ at $k = 2.9$ (wavelength 220 km). Modes $T_1$, $T_2$, and $T_3$ have their maximum amplitudes at 450-, 350-, and 550-hPa levels (Table 1), respectively. Their amplitudes decrease rapidly to less than 1/50 of the maximum at the adjacent levels.[2] The top of the cloud band $\beta$ was 450 hPa, and mode $T_1$ has the maximum amplitude at this level. Its phase velocity is 26.5 m s$^{-1}$ and agrees well with the observed translational speed of the vortices (30.0 m s$^{-1}$).

Figure 17 shows the horizontal velocity field of mode $T_1$ at the 450-hPa level. The center of the circulation of the mode $T_1$ is in the region where the vorticity of the basic-state flow is negative (anticyclonic). Though the velocity perturbation field in Fig. 17 consists of a series of alternating positive and negative vorticities, the dominant negative vorticity in the basic state masks the positive vorticity perturbation. The total vorticity is negative everywhere (e.g., Michalke 1965).

### c. Stability of one-dimensional profile

The characteristics of barotropically unstable waves can be sensitive to the grid size and the location of the boundaries. For example, to obtain a realistic behavior of the waves, the boundaries must be located far from the shear zone ($b \gg 1$) and the grid size must be sufficiently small. Yanai and Nitta (1968) concluded that the instability of a sine profile flow between rigid walls should be calculated with at least 20 grid points. Niino (1982) showed that the eigenvalue for the instability of a tanh$y$ flow is subject to an error of about 20% for $b = 3$, and 2% for $b = 6$. For the stability of the two-

[2] To check a possible problem in the vertical resolution, the same calculation except with 20 grid points in the vertical direction was made. The instability characteristics differ very little from those presented in Figs. 15–17.

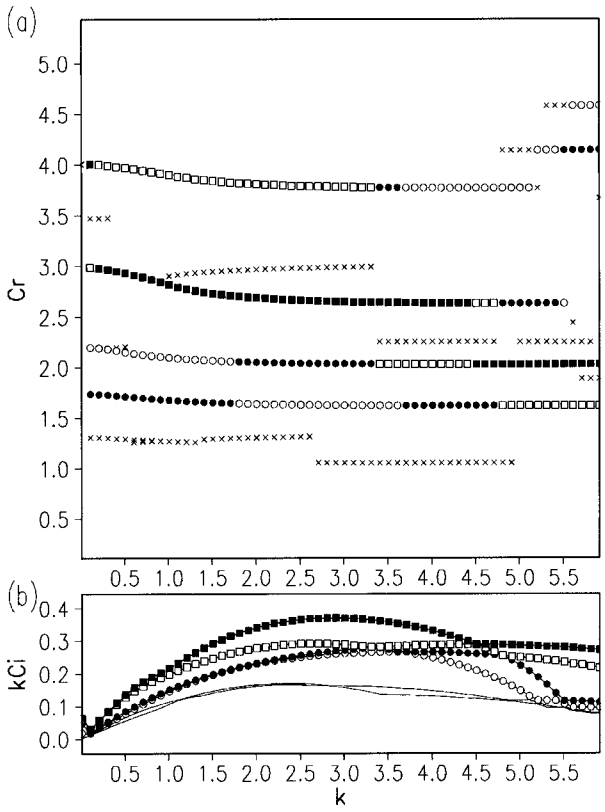


FIG. 15. Dispersion relation of principal six modes for the two-dimensional problem; (a) phase speed $c_r$ and (b) growth rate $kc_i$.

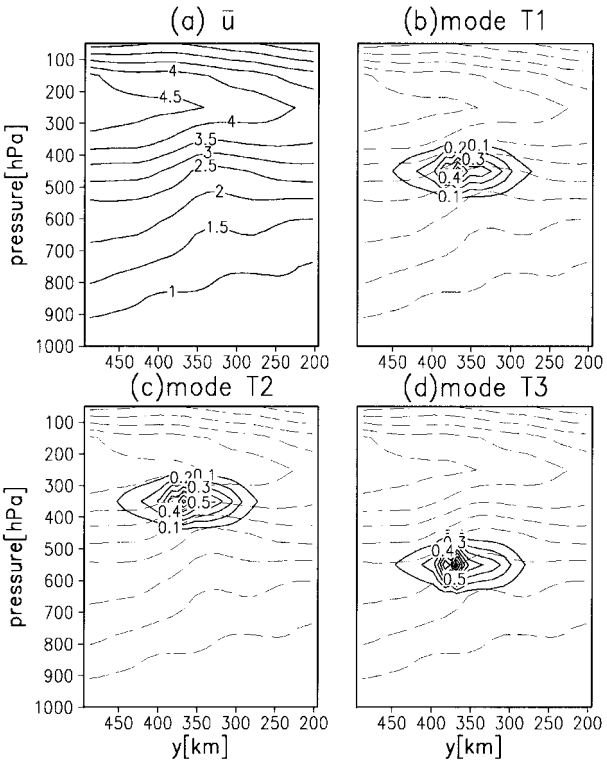


FIG. 16. Vertical structure of the principal three modes in the two-dimensional problem; (a) nondimensional velocity of the basic field; (b) horizontal disturbance velocity for mode $T_1$ at wavenumber $k = 2.9$; (c) same as (b) except for mode $T_2$; and (d) same as (b) except for mode $T_3$.

dimensional profile examined in the previous section, limitations on computer resources forced us to take only 20 horizontal grid points between $b = \pm 1.5$.

In order to examine in more detail the characteristics of modes $T_1$ and $T_6$, which have the largest amplitude at the 450-hPa level (the top level of the cloud band $\beta$), the barotropic instability of the one-dimensional wind profile at this level is examined in this section. The formulation of the stability problem is the same as that in the previous section except that the number of the vertical grid points was reduced to one. Figure 18 shows the wind profile of the basic field. Since the one-dimensional problem does not involve thermodynamics, no information on the temperature distribution of a basic field is required.

TABLE 1. Characteristics of the principal modes in the two-dimensional model. Here $C(\overline{K}, K')_Y$, $C(\overline{K}, K')_P$, $C(A', K')$, and $C(\overline{A}, A')$ denote energy conversion rates from the kinetic energy (KE) of the horizontal shear of the basic flow to that of the perturbation, from KE of the vertical shear of the basic flow to KE of the perturbation, from the available potential energy (APE) of the perturbation to KE of the perturbation, and from APE of the basic field to APE of the perturbation, respectively. The conversion rates are scaled by total production rate of the perturbation energy, $C(\overline{A}, A') + C(\overline{K}, K')_Y + C(\overline{K}, K')_P$. Each energy conversion rate is mathematically defined in appendix B.

| Parameter | (Units) | Mode name | | | | |
|---|---|---|---|---|---|---|
| | | $T_1$ | $T_2$ | $T_3$ | $T_4$ | $T_6$ |
| Level of max amplitude | (hPa) | 450 | 350 | 550 | 650 | 450 |
| Wavelength of max growth rate | (km) | 220 | 230 | 140 | 170 | 260 |
| Min *e*-folding time | (h) | 7.50 | 9.51 | 9.58 | 10.4 | 16.7 |
| | | For wavelength 220 km: | | | | |
| Phase velocity | (m s$^{-1}$) | 26.5 | 37.8 | 20.4 | 16.3 | 29.9 |
| *e*-folding time | (h) | 7.50 | 9.56 | 10.3 | 10.7 | 17.2 |
| $C(\underline{\overline{K}}, K')_Y$ | Relative | 0.966 | 0.922 | 0.973 | 0.975 | 0.904 |
| $C(\overline{K}, K')_P$ | Relative | 0.031 | 0.079 | 0.029 | 0.025 | 0.097 |
| $C(\underline{A'}, K')$ | Relative | −0.004 | −0.002 | −0.002 | −0.003 | −0.003 |
| $C(\overline{A}, A')$ | Relative | 0.003 | −0.002 | −0.002 | 0.000 | −0.001 |

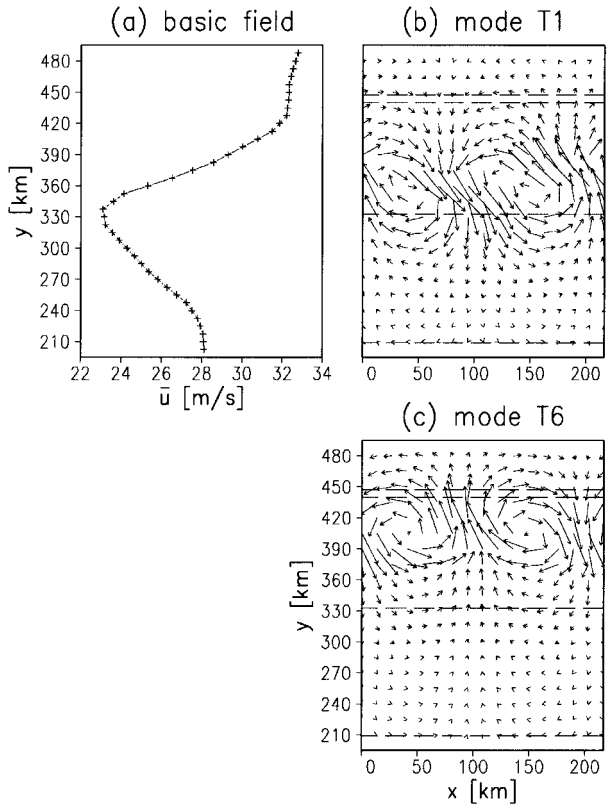


FIG. 17. Horizontal velocity fields of modes that have maximum amplitude at the 450-hPa level; (a) nondimensional wind speed of the basic field; (b) horizontal disturbance velocity of mode $T_1$ at the 450-hPa level and wavenumber $k = 2.9$; (c) same as (b) except for mode $T_6$. Broken lines denote the line of $\partial_y \overline{u} = 0$.

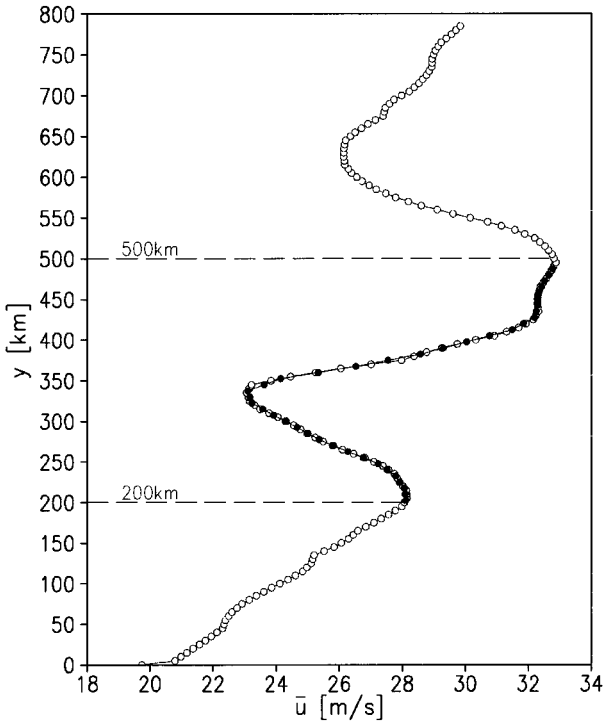


FIG. 18. Wind profile in the basic state for the one-dimensional model (80 and 20 grids). Horizontal dashed lines denote the domain shown in Fig. 20.

In order to confirm that the modes $T_1$ and $T_6$ can be well reproduced by the one-dimensional model, the grid interval and the location of the boundaries were first set to be the same values as the two-dimensional problem. The characteristics of the two modes with the largest growth rates are shown in Table 2. Mode $R_1$ has the smallest *e*-folding time of 7.56 h and a phase velocity of 26.5 m s$^{-1}$ at a wavelength of about 210 km. These characteristics agree well with those of the mode $T_1$ in the two-dimensional model. The horizontal structure of mode $R_1$ is very similar to that of mode $T_1$ (not shown). A similar correspondence between mode $R_2$ and mode $T_6$ are also found. Thus, the barotropic instability problem of the one-dimensional wind profile at the 450-hPa level reproduces the characteristics of the disturbance, which has the maximum amplitude at the 450-hPa level, in the two-dimensional model.

Now, to examine the influence of the boundary and the grid size, the one-dimensional problem was solved with 80 grid points and boundaries at $y = 0$ km and $y = 800$ km (shown in Fig. 18). Since the grid interval is 10 km, the weak wind region, the width of which is 200 km, is resolved satisfactorily with 20 grid points. The nondimensional width $b$ of the calculation domain becomes 4.

Figure 19 shows the dispersion relation. The characteristics of the principal modes that have the first to third largest growth rate are shown in Table 3. Mode $P_1$ has the smallest *e*-folding time of 8.57 h at a wavelength of 210 km. This *e*-folding time is quite close to that of mode $T_1$.

The horizontal structure of mode $P_1$ (Fig. 20) is also nearly similar to that of mode $T_1$ (Fig. 17) for the two-dimensional model and we think that mode $P_1$ corresponds to modes $T_1$ and $R_1$. The second fastest growing mode $P_2$ seems to be caused by a weak wind region in the vicinity of $y = 620$ km (associated with cloud band $\gamma$). Its growth rate at a wavelength of about 200 km is very small. The characteristics of the third fastest growing mode $P_3$ are similar to those of mode $T_6$ and $R_2$.

TABLE 2. Characteristics of the principal modes in the one-dimensional problem with 20 grid points.

| Parameter | (Units) | Mode name $R_1$ | Mode name $R_2$ |
|---|---|---|---|
| Wavelength of max growth rate | (km) | 210 | 260 |
| Min *e*-folding time | (h) | 7.56 | 18.8 |
| For wavelength of 210 km: | | | |
| Phase velocity | (m s$^{-1}$) | 26.5 | 29.8 |
| *e*-folding time | (h) | 7.56 | 20.1 |

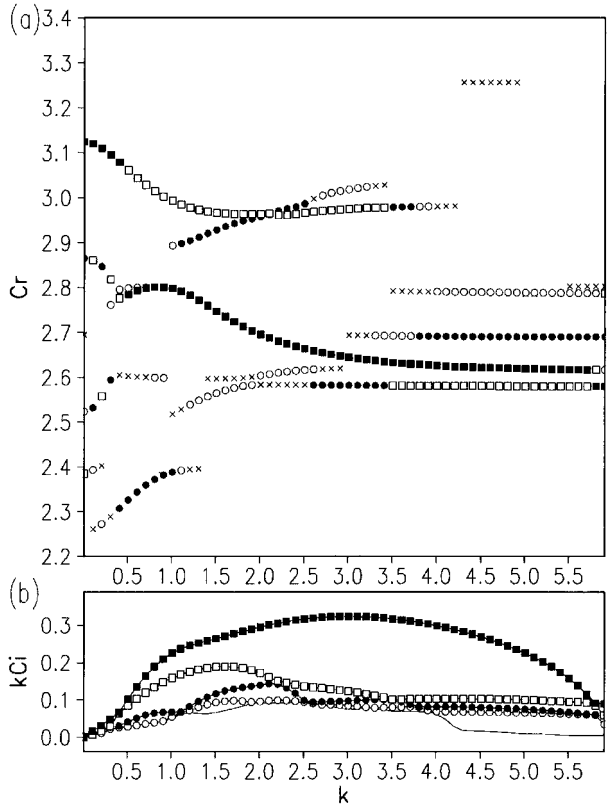


FIG. 19. Dispersion relation of principal six modes for the one-dimensional model with 80 grid points. Axes and symbols are the same as in Fig. 15.

On the other hand, the *e*-folding time of the fastest growing mode turned out to be about 7–9 h. Since the vortex street in the satellite picture (Fig. 2) developed quickly in 6 h, however, it is likely that the *e*-folding time of the disturbance in the real atmosphere is shorter than at most 6 h.

We think that the smaller growth rate in the linear stability theory is caused by the smaller horizontal shear of wind across the weak wind region in the numerical model output. The characteristic *e*-folding time of the barotropically unstable disturbance is scaled by $U/L$, where $U$ is the velocity deficit in the weak wind region and $L$ is a characteristic width of the weak wind region. Actually, the velocity deficit in the weak wind region in the sounding at Naha was about 15 m s$^{-1}$, though that in the numerical simulation was only 10 m s$^{-1}$ (Fig. 18).

## 5. Discussion

### *a. Vertical transport of momentum by convection*

As shown in section 3d, the weak wind region in the numerical model is formed by vertical advection of horizontal momentum by the convective cloud band, which is resolved in the 15-km mesh model.

TABLE 3. Characteristics of the principal modes in the one-dimensional model with 80 grid points.

| Parameter | (Units) | Mode name $P_1$ | $P_2$ | $P_3$ |
|---|---|---|---|---|
| Wavelength of max growth rate | (km) | 210 | 390 | 290 |
| Min *e*-folding time | (h) | 8.57 | 14.7 | 18.4 |
| For wavelength of 210 km: | | | | |
| Phase velocity | (m s$^{-1}$) | 26.4 | 29.6 | 29.6 |
| *e*-folding time | (h) | 8.57 | 33 | 22.6 |
| Growth rate order | | 1 | 4 | 2 |

There have been a number of studies about vertical transport of horizontal momentum by convective clouds (e.g., Newton and Newton 1959; Fankhauser 1971). The mixing by convection has been thought to cause a downgradient transport of momentum. However, LeMone's (1983) observational study using an aircraft showed that, while momentum parallel to cloud line is transported downgradient, momentum normal to cloud line is transported upgradient. Moncrieff (1981) proposed a dynamical model to explain this feature. LeMone and Moncrieff (1994) showed that the model is compatible with observations.

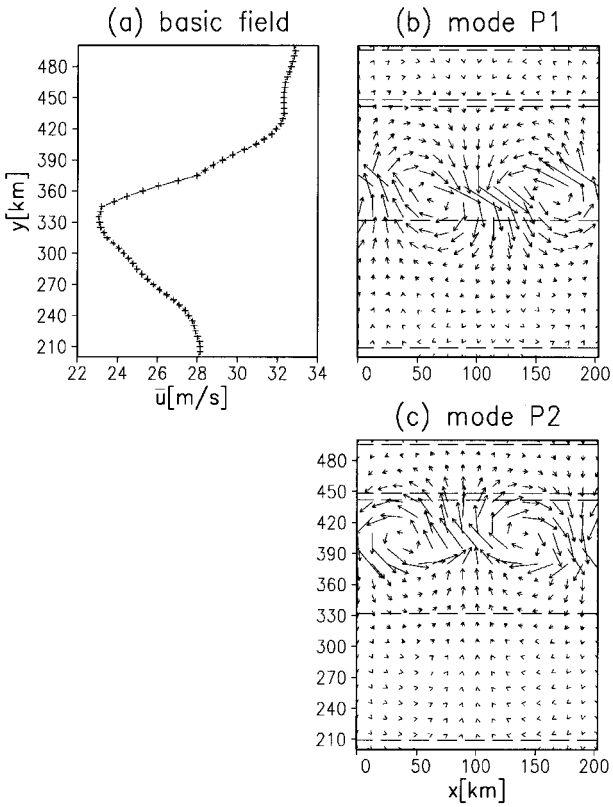


FIG. 20. Horizontal velocity fields for modes $P_1$ and $P_3$ for the one-dimensional model with 80 grid points and wavenumber $k = 3.0$. Axes and symbols are the same as in Fig. 17. The same area as Fig. 17 is shown for the sake of comparison, though the whole calculation domain is much wider (Fig. 18).

In the present numerical model, the vertical transport of horizontal momentum is expressed merely by the advection, and horizontal momentum in both the along-front and cross-front directions is transported downgradient. The hydrostatic approximation and large grid size may also affect the nature of simulated convective band. However, the weak wind region of the present study is of along-front wind, and the along-front momentum is transported downgradient. In the present study, the maximum deceleration due to vertical advection was 2 m $s^{-1}$ $h^{-1}$. In the previous observations (e.g., LeMone and Moncrieff 1994; Wu and Yanai 1994), the estimated decelerations by convection range from 1 to 30 m $s^{-1}$ $h^{-1}$. Therefore, the deceleration obtained from the present numerical simulation is not unrealistic.

### b. *Vertical structure of barotropically unstable disturbance*

The amplitudes of the fastest growing modes, which have been obtained in section 4b, were confined to a thin layer. Killworth (1980) theoretically studied the vertical structure of a barotropically unstable disturbance in a zonal flow that varies both in the cross-stream and vertical directions. If the vertical shear of the basic velocity field is negligible in comparison to the horizontal shear, the disturbance becomes barotropic when the ratio $\lambda \equiv L/a$ is much less than unity, where $L$ is the horizontal length scale of the basic flow and $a$ is the Rossby internal radius of deformation. The amplitude is proportional to $\exp[-\alpha(z - z_0)^2\lambda^{-1}]$ and the phase oscillates vertically on the scale of $O(\lambda)$, where the vertical length scale is taken to be unity.

If we take the scale height $H$ for the vertical length scale, Rossby's internal radius of deformation ($NH/f$, where $N$ is buoyancy frequency) is about 1000 km in the vicinity of 450 hPa. Since the horizontal length scale of the basic state in the present study is 100 km, $\lambda = 0.1$. Although the characteristic depth of the disturbance predicted by Killworth's solution is $O(\lambda^{1/2}) \sim 0.3$, which is about 300 hPa, our result in section 4 shows that the disturbance is much thinner. In the present study, however, nondimensionalized $\partial_y\overline{u}$ and $\partial_p\overline{u}$ are of the same order. Since the result of Killworth was obtained under the assumption that the vertical shear is small enough in comparison to the horizontal shear

$$\frac{|\partial_p \overline{u}|}{|\partial_y \overline{u}|} \lesssim O(\lambda),$$

our result does not necessarily contradict his result.

### c. *Horizontal transport of momentum by barotropic instability disturbance*

The most prominent vortex in the present analysis appeared at (23°N, 124°E) about 1200 UTC 11 April 1995. The vortex developed to a diameter of 70 km at 1600 UTC and the cloud surrounding the vortex rotated anticyclonically about 180° during 4 h (Fig. 2). If the cloud is assumed to be advected 100 km (length of semicircle) by the vortex flow, the characteristic velocity of the disturbance may be estimated to be about 10 m $s^{-1}$.

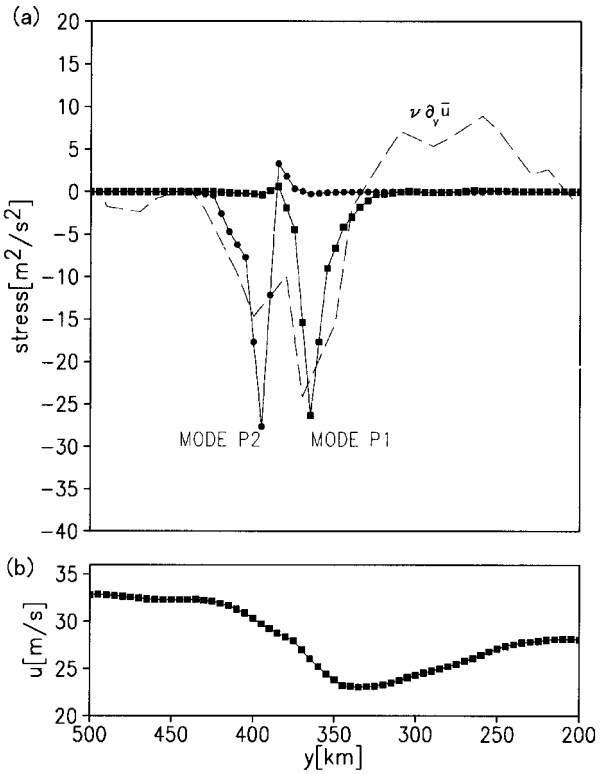


FIG. 21. (a) Reynolds stress $\overline{u'v'}$ ($m^2$ $s^{-2}$) for modes $P_1$ (solid square) and $P_3$ (solid circle) obtained from the one-dimensional (80 grids) model. Amplitude of the modes is scaled in the way that the maximum horizontal wind speed becomes 10 m $s^{-1}$. Dashed line denotes the eddy viscosity stress $\nu\partial_y\overline{u}$, which is obtained from the wind shear of basic field $\partial_y\overline{u}$. The eddy viscosity is assumed to be $\nu = 2.5 \times 10^4$ $m^2$ $s^{-1}$. (b) The wind speed of basic field (m $s^{-1}$).

If the two modes $P_1$ and $P_3$ in section 4c are assumed to have a perturbation horizontal wind of 10 m $s^{-1}$ near the weak wind region at $y = 350$ km, the Reynolds stress due to the modes may be calculated. The results are shown in Fig. 21. The dashed line in the figure, on the other hand, shows an eddy momentum flux $-\nu\partial_y\overline{u}$ estimated from the basic flow $\overline{u}$ with a constant eddy viscosity $\nu$ of $2.5 \times 10^5$ $m^2$ $s^{-1}$. It is seen that the Reynolds stress estimated from the eddy viscosity formulation is $2.5 \times 10^5$ $m^2$ $s^{-1}$. This value of the eddy viscosity is somewhat larger than the horizontal viscosity $\nu_M \equiv 5.3 \times 10^4$ $m^2$ $s^{-1}$ used in the numerical model of section 3. This suggests that, if barotropically unstable disturbances of this kind occur frequently in the atmosphere, they may play an important role in the horizontal diffusion of momentum and materials.

*d. Lack of vortices in the simulation*

In section 3, the weak wind region was generated 20 h after the start of integration, and the integration was continued for an additional 16 h. Though the *e*-folding time of the fastest growing mode disturbance in the two-dimensional wind profile is about 7 h, we did not detect such a disturbance in the numerical simulation. We think that the difference in the behavior of the disturbances between our theory and the simulation model was caused by the use of horizontal diffusion in the model.

In most free shear flows, viscosity stabilizes the barotropic instability. Let us define a Reynolds number Re $\equiv (UL/\nu)$, where $U$ is half the velocity difference across the shear flow and $L$ is the width of the shear zone. When the shear flow on the north side of the weak wind region is regarded as a free shear layer, $U \sim 5$ m s$^{-1}$, $L \sim 100$ km, and $\nu = \nu_M$. This gives a Reynolds number of 10. For a free shear layer of the $\overline{u} = \tanh y$ type, the maximum growth rate for Re $= 10$ is about half of that of the inviscid case (Betchov and Szewczyk 1963). Therefore, the disturbance does not seem to amplify during the simulation time.

## 6. Summary and conclusions

The characteristics, formation mechanisms, and environmental fields of a meso-$\beta$-scale anticyclonic vortex street that appeared along a cold front near the Ryukyu Islands on 11 April 1995 were studied. The vortex street occurred along the north edge of a cloud band along the cold front. Each individual vortex had a diameter of 70 km, and a lifetime of about 6 h. The spacing between two vortices was 100–200 km. The clouds associated with the vortices were at a height of 300–700 hPa. The translational speed of the vortices was nearly equal to the wind speed near 400 hPa.

The cloud band had a convective region with strong precipitation at its southwest edge. Since the clouds that visualized the vortices were nonprecipitating, it is likely that cloud particles in the vortices simply played a role of tracers of the midtropospheric wind. The upper-air observations indicate that the cloud band was accompanied by a weak wind region in the midtroposphere. The deficit of the along-front wind speed in the weak wind region was about 15 m s$^{-1}$. A region of very large anticyclonic vorticity ($\sim 10^{-4}$ s$^{-1}$) existed on the north side of the weak wind region. In the middle of the region with anticyclonic vorticity, the gradient of the potential vorticity vanished.

To examine a detailed structure and the formation mechanism of this weak wind region, a numerical simulation was performed. The convective cloud band and the associated weak wind region were well simulated. An examination of terms in the along-front momentum equation revealed that the weak wind region was mainly produced by the vertical advection of horizontal momentum by the convective band, which was expressed in the 15-km mesh model.

The stability of the simulated along-front wind and temperature fields near the weak wind region was examined by a linear theory. It was found that there exist a number of growing modes, the disturbance kinetic energy of which is supplied by the kinetic energy of the basic flow (i.e., barotropic instability). The fastest growing mode has a maximum amplitude at 450 hPa and its amplitude is confined to the region of 450 hPa $\pm$ 100 hPa. The wavelength and the phase velocity of the fastest growing mode agree reasonably well with the observed characteristics of the vortex street.

This paper has presented the first evidence that the vertical transport of horizontal momentum by a convective cloud band can lead to barotropic instability. The vortices caused by the barotropic instability, in turn, transport considerable momentum in the horizontal direction.

In the present case, the vortices happened to be made visible by cloud particles. It is, however, of interest to know how frequently these vortices occur in the atmosphere. Geostationary Meteorological Satellite *GMS-5*, whose operation started in June 1995, gives ''water vapor images'' of wavelength of 6.5–7.0 $\mu$m. The water vapor images are capable of visualizing the mid- and upper-troposphere flows and may be used to answer this question in the future.

*Acknowledgments.* This paper is part of M.S. thesis of E.T. submitted to the Department of Earth and Planetary Physics, University of Tokyo. We would like to express special thanks to Drs. A. Segami and H. Tada of JMA and staff members of the Numerical Prediction Division of JMA for their support. We are also grateful to anonymous referees for their helpful comments on the original manuscript. The simulations and calculations were performed using the HITAC S3800 supercomputer, the M880 computer at the Computer Center of the University of Tokyo, and the IBM PowerSTATION RS6000/590 at the Ocean Research Institute of the University of Tokyo. The Grid Analysis and Display System developed at COLA, University of Maryland, was used for displaying data and drawing figures. A terminal emulator *eriot* developed by Prof. Kazuki Koketsu of the Earthquake Research Institute, University of Tokyo, was used for connecting to the Computer Center. We thank Dr. K. Iga, the Research Institute for Applied Mechanics, Kyushu University, for helpful advice in the numerical study of the linear stability theory.

## APPENDIX A

### Numerical Procedure to Solve Linear Eigenvalue Problem

Assuming that the dimensionless Eqs. (11)–(15) have a solution of the waveform (18), we can rewrite them by putting $\partial_t = -ikc$ and $\partial_x = ik$:

$$iku + \partial_y v + \partial_p \omega = 0 \quad \text{(A1)}$$

$$ik(\overline{u} - c)T + v\partial_y \overline{T} - \overline{S}\omega = 0 \quad \text{(A2)}$$

$$\mathrm{Ro}[ik(\overline{u} - c)\,\mathrm{u} + v\partial_y \overline{u} + \omega\partial_p \overline{u}] - v = -ik\Phi \quad \text{(A3)}$$

$$ik\mathrm{Ro}(\overline{u} - c)v + u = -\partial_y \Phi \quad \text{(A4)}$$

$$\partial_p \Phi = -\frac{T}{p}. \quad \text{(A5)}$$

These equations together with the boundary conditions (16) and (17) constitute an eigenvalue problem for eigenvalue $c$. Using Eqs. (A1) and (A5), we can eliminate $u$ and $T$ and obtain the following equations in terms of $v$, $\omega$, and $\Phi$:

$$-(\overline{u} - c)p\partial_p \phi + v\partial_y \overline{T} - \omega\overline{S} = 0 \quad \text{(A6)}$$

$$\mathrm{Ro}[-(\overline{u} - c)(\partial_y v + \partial_p \omega) + v\partial_y \overline{u} + \omega\partial_p \overline{u}] - v = -\phi \quad \text{(A7)}$$

$$\mathrm{Ro}k^2(\overline{u} - c)v + (\partial_y v + \partial_p \omega) = \partial_y \phi, \quad \text{(A8)}$$

where a new variable $\phi \equiv ik\Phi$ was defined to make all coefficients real. These manipulations reduce the size of the matrix for solving the eigenvalue problem by about 30% and save memory and calculation time greatly.

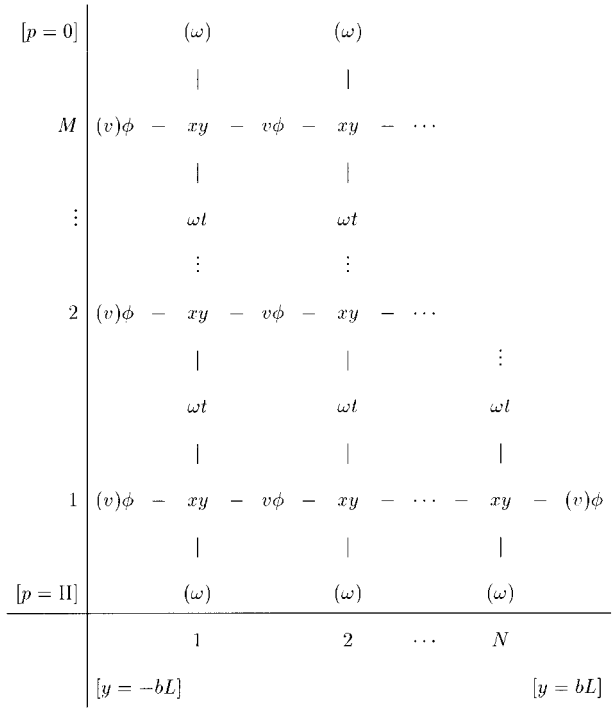


FIG. A1. Grid arrangement for solving the eigenvalue problem: *xy*, grid points where the equation of motions in the $x$ and $y$ directions [(A7), (A8)] are evaluated; *t*, grid points where the thermodynamic equation [(A6)] is evaluated; $v$, $\omega$, $\phi$, grid points where these variables are evaluated. Parenthesized variable symbol means that the variable vanishes because of the boundary condition.

The eigenvalue problem (A6)–(A8) is solved by replacing differentiation operators with finite differences, where the grid arrangement is shown in Fig. A1. There are two advantages of using this grid arrangement. First, since the equations of motion in the $x$ and $y$ directions are evaluated at the same point, the resolution of the basic field given by the grid is not lost. Second, if the number of grid points in the vertical direction is set equal to 1, it easily reduces to the barotropic instability problem for the one-dimensional wind profile.

In the following, the number of grid points in the vertical and horizontal directions will be denoted as $M$ and $N$, respectively. The degrees of freedom of the system (the number of variables) is $3MN - N$, and $3MN - N$ linear equations are obtained by the finite difference method from the eigenvalue problem (A6)–(A8). This equation system can be written as

$$(A - cB)\mathbf{x} = 0, \quad \text{(A9)}$$

where $\mathbf{x}$ is a vector of $3MN - N$ variables; $A$ and $B$ are matrices of the $(3MN - N)$-th order, which are functions of Ro, $\overline{S}$, $\overline{u}$, $\partial_y \overline{u}$, and $\partial_p \overline{u}$, and $k$. Eigenvalues $c$ and eigenvectors $\mathbf{x}$ can be obtained by solving the eigenvalue problem (A9).

## APPENDIX B

### Energy Conversion Rate in Linear Theory

Let us consider the energy budget for the disturbance and the basic field in the linear theory. The prime sign ($'$) to denote disturbance quantities will not be suppressed here.

The kinetic energy (KE) and the available potential energy (APE) of the basic field and the disturbance for unit volume are defined, respectively, as follows:

KE of the basic field,

$$\overline{K} \equiv \frac{1}{2g}\int_y \int_p (\overline{u}^2 + \overline{v}^2)\, dp\, dy; \quad \text{(B1)}$$

KE of the disturbance,

$$K' \equiv \frac{1}{2g}\int_y \int_p (\overline{u'^2} + \overline{v'^2})\, dp\, dy; \quad \text{(B2)}$$

APE of the basic field,

$$\overline{A} \equiv \frac{1}{g}\int_y \int_p \frac{R}{2p\langle S\rangle}\overline{T''}^2\, dp\, dy; \quad \text{(B3)}$$

APE of the disturbance,

$$A' \equiv \frac{1}{g}\int_y \int_p \frac{R}{2p\langle S\rangle}\overline{T'^2}\, dp\, dy; \quad \text{(B4)}$$

where the bracket ($\langle\ \rangle$) denotes an average over an isobaric plane, the double prime ($''$) denotes a deviation from the isobaric average, $\langle S\rangle \equiv R\langle T\rangle/(c_p p) - \partial_p\langle T\rangle$ is the average stability in pressure coordinate, and

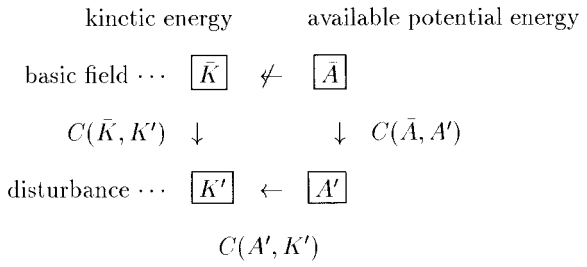


FIG. B1. Relations among the basic and disturbance energies, and energy conversion rates.

$$\int_y dy \equiv \frac{1}{2bL}\int_{-bL}^{bL} dy, \qquad \int_p dp \equiv \frac{1}{\Pi}\int_0^{\Pi} dp.$$

The equations for the rate of change of these energies can be obtained from the governing system (2)–(6) as follows. Nondimensionalize the equations of motion [(3), (4)] and thermodynamic equation [(6)] in the same way as in section 4a. Multiply the equations of motion by $\overline{u}$ or $u'$ and thermodynamic equation by $\overline{T''}$ or $T'$, and integrate them in the $x$, $y$, and $p$ directions over the entire region. The terms $\partial_p(R/p\langle S\rangle)$ and $R\overline{T''}/(c_p p\langle S\rangle)$, and third-order correlation terms such as $\overline{u'v'}\partial_y\overline{u'}$, are ignored. The third-order correlation term is ignored commonly (e.g., Ogura 1978). Simplifying the equations with the aid of the continuity equation [(2)], periodicity of disturbance in the $x$ direction, and boundary conditions (9) and (10), we obtain finally

$$\partial_t\overline{K} = -C(\overline{K}, K'), \tag{B5}$$

$$\partial_t K' = C(\overline{K}, K') + C(A', K'), \tag{B6}$$

$$\partial_t\overline{A} = -C(\overline{A}, A'), \tag{B7}$$

$$\partial_t A' = C(\overline{A}, A') - C(A', K'), \tag{B8}$$

where

$$C(A', K') \equiv -\int_y\int_p \frac{R}{p}\overline{T'\omega'}\, dp\, dy$$

is a conversion rate from APE of the disturbance to KE of the disturbance;

$$C(\overline{K}, K') \equiv -\int_y\int_p (\overline{u'v'}\partial_y\overline{u} + \overline{u'\omega'}\partial_p\overline{u})\, dp\, dy$$

is a conversion rate from KE of the basic field to KE of the disturbance; and

$$C(\overline{A}, A') \equiv -\int_y\int_p \frac{R}{p\langle S\rangle}(\overline{v'T'}\partial_y\overline{T}'' + \overline{\omega'T'}\partial_p\overline{T}'')\, dp\, dy$$

is a conversion rate from APE of the basic field to APE of the disturbance. Conversion from the potential energy of the basic state to the kinetic energy of the basic state does not occur within the framework of the linear theory. Figure B1 shows relations among energies and their conversion rates. Since the amplitude of the disturbance is not determined from the linear theory, only ratios among energy conversion rates have a meaning. Tables 1–3 show energy conversion rates, scaled by the total energy conversion rate $C(\overline{A}, A') + C(\overline{K}, K')$ from the basic state to the disturbance.

The kinetic energy conversion rate $C(\overline{K}, K')$ from the basic state to the disturbance can be divided into that by the horizontal shear and that by the vertical shear, and they are given by

$$C(\overline{K}, K')_Y \equiv -\int_y\int_p \overline{u'v'}\partial_y\overline{u} \quad \text{and}$$

$$C(\overline{K}, K')_P \equiv -\int_y\int_p \overline{u'\omega'}\partial_p\overline{u},$$

respectively.

## REFERENCES


Akaeda, K., and H. Sakakibara, 1996: Heavy rain caused by a tapering cloud (in Japanese). *Proc. Meeting on Formation Process of Cloud System Which Causes Heavy Rain,* Nagoya, Japan, Institute for Hydrospheric-Atmospheric Sciences, Nagoya University, 55–68.

Asai, T., 1988: Meso-scale features of heavy snowfalls in Japan Sea coastal regions of Japan (in Japanese). *Tenki,* **35,** 156–161.

——, and Y. Miura, 1981: An analytical study of meso-scale vortex-like disturbances observed around Wakasa bay area. *J. Meteor. Soc. Japan,* **59,** 832–843.

Betchov, R., and A. Szewczyk, 1963: Stability of a shear layer between parallel streams. *Phys. Fluids,* **6,** 1391–1396.

Case, K. M., 1960: Stability of inviscid plane Couette flow. *Phys. Fluids,* **3,** 143–148.

Fankhauser, J. C., 1971: Thunderstorm-environment interactions determined from aircraft and radar observations. *Mon. Wea. Rev.,* **99,** 171–192.

Fujita, T. T., 1963: Analytical mesometeorology: A review. *Severe Local Storms, Meteor. Monogr.,* No. 27, Amer. Meteor. Soc., 77–125.

Gadd, A. J., and J. F. Keers, 1970: Surface exchanges of sensible and latent heat in a 10-level model atmosphere. *Quart. J. Roy. Meteor. Soc.,* **96,** 297–308.

Hino, M., 1992: *Fluid Mechanics* (in Japanese). Asakura Shoten, 469 pp.

Hubert, L. F., and A. F. Krueger, 1962: Satellite pictures of mesoscale eddies. *Mon. Wea. Rev.,* **90,** 457–463.

Itoh, H., T. Asoh, and M. Sakurada, 1992: Meteorological conditions that lead to an occurrence of a tapering cloud and its appearance on the GMS image (in Japanese). *Tech. Rep. Meteor. Satellite Center,* **24,** 1–8.

Kibe, S., and T. Matsumoto, 1989: Analysis of a rope-shaped echo (in Japanese). *Geophys. Notes Sapporo District Meteor. Obs.,* **38**(extra issue), 99–103.

Killworth, P. D., 1980: Barotropic and baroclinic instability in rotating stratified fluids. *Dyn. Atmos. Oceans,* **4,** 143–184.

LeMone, M. A., 1983: Momentum transport by a line of cumulonimbus. *J. Atmos. Sci.,* **40,** 1815–1834.

——, and M. W. Moncrieff, 1994: Momentum and mass transport by convective bands: Comparisons of highly idealized dynamical models to observations. *J. Atmos. Sci.,* **51,** 281–305.

Lyons, S. W., 1988: Development of mesoscale vortices along a subtropical frontal remnant. *Mon. Wea. Rev.,* **116,** 485–488.

Mellor, G. L., and T. Yamada, 1974: A hierarchy of turbulence closure

models for planetary boundary layers. *J. Atmos. Sci.,* **31,** 1791–1806.
Michalke, A., 1965: Vortex formation in a free boundary layer according to stability theory. *J. Fluid Mech.,* **22,** 371–383.
Miyazawa, S., 1967: On vortical meso scale disturbances observed during the period of heavy snow or rain in the Hokuriku district. *J. Meteor. Soc. Japan,* **45,** 166–176.
Moncrieff, M. W., 1981: A theory of organized steady convection and its transport properties. *Quart. J. Roy. Meteor. Soc.,* **107,** 29–50.
Muramatsu, T., 1971: On periodic change of surface wind in Wakkanai districts in Hokkaido (in Japanese). *Tenki,* **18,** 307–313.
Nagata, M., 1993: Meso-$\beta$-scale vortices developing along the Japan-sea polar-airmass convergence zone (JPCZ) cloud band: Numerical simulation. *J. Meteor. Soc. Japan,* **71,** 43–57.
Newton, C. W., and H. R. Newton, 1959: Dynamical interactions between large convective clouds and environment with vertical shear. *J. Meteor.,* **16,** 483–496.
Niigata Local Meteorological Observatory, 1972: Anti-cyclonic vortex echo (in Japanese). *Tech. Note Tokyo District Meteor. Obs.,* **28,** cover page.
Niino, H., 1982: A weakly non-linear theory of barotropic instability. *J. Meteor. Soc. Japan,* **60,** 1001–1023.
Ninomiya, K., and K. Hoshino, 1990: Evolution process and multi-scale structure of a polar low developed over the Japan Sea on 11–12 December 1985, Part II: Meso-$\beta$-scale low in meso-$\alpha$-scale polar low. *J. Meteor. Soc. Japan,* **68,** 307–318.
Nyuda, H., 1974: Radar and meso-scale analysis on anti-cyclonic vortical radar echo (in Japanese). *Tenki,* **21,** 207–213.
Ogura, Y., 1978: *Principles of Atmospheric Dynamics.* University of Tokyo Press, 249 pp.
——, and T. Takahashi, 1971: Numerical simulation of the life cycle of a thunderstorm cell. *Mon. Wea. Rev.,* **99,** 895–911.
Ookubo, A., 1995: Two types of vortical disturbances over the Hokuriku district in winter (in Japanese). *Tenki,* **42,** 705–714.
Orlanski, I., 1975: A rational subdivision of scale for atmospheric processes. *Bull. Amer. Meteor. Soc.,* **56,** 255–266.
Schär, C., and D. R. Durran, 1997: Vortex formation and vortex shedding in continuously stratified flows past isolated topography. *J. Atmos. Sci.,* **54,** 534–554.
Segami, A., K. Kurihara, H. Nakamura, M. Ueno, I. Takano, and Y. Tatsumi, 1989: Operational mesoscale weather prediction with Japan Spectral Model. *J. Meteor. Soc. Japan,* **67,** 907–924.
Tatsumi, Y., 1986: A spectral limited-area model with time-dependent lateral boundary conditions and its application to a multi-level primitive equation model. *J. Meteor. Soc. Japan,* **64,** 637–664.
Tsuchiya, K., 1969: The clouds with the shape of Kármán vortex street in the wake of Cheju Island, Korea. *J. Meteor. Soc. Japan,* **47,** 457–465.
Wu, X., and M. Yanai, 1994: Effects of vertical wind shear on the cumulus transport of momentum: Observations and parameterization. *J. Atmos. Sci.,* **51,** 1640–1660.
Yanai, M., and T. Nitta, 1968: Finite difference approximations for the barotropic instability problem. *J. Meteor. Soc. Japan,* **46,** 389–403.
Yasuda, M., 1974: On the vertical echo and the eye associated with mesoscale cyclone, observed by Naze radar (in Japanese). *Tenki,* **21,** 203–206.